



# Proximity of defects and Ti-H on hydrogenated SrTiO<sub>3</sub> mediated photocatalytic reduction of CO<sub>2</sub> to C<sub>2</sub>H<sub>2</sub>

Haiying Xu <sup>a</sup>, Zhaoliang Wang <sup>a</sup>, Hehua Liao <sup>a</sup>, Dongmiao Li <sup>a</sup>, Jinni Shen <sup>a,\*</sup>, Jinlin Long <sup>a</sup>, Wenxin Dai <sup>a,b</sup>, Xuxu Wang <sup>a</sup>, Zizhong Zhang <sup>a,b,\*\*</sup>

<sup>a</sup> State Key Laboratory of Photocatalysis on Energy and Environment, College of Chemistry, Fuzhou University, Fuzhou 350106, PR China

<sup>b</sup> Qingyuan Innovation Laboratory, Quanzhou 362801, PR China



## ARTICLE INFO

**Keywords:**  
CO<sub>2</sub> reduction  
C-C coupling  
Photocatalysis  
Ti-H species  
Defect sites

## ABSTRACT

Photocatalytic converting CO<sub>2</sub> into C<sub>2</sub> products is highly desirable but is extremely sensitive to catalyst structure. In this work, Ti-H species and oxygen vacancies are simultaneously integrated on hydrogenated SrTiO<sub>3</sub> surface by thermally treating with NaBH<sub>4</sub>, which promotes the activation of CO<sub>2</sub> into HCOO<sup>-</sup> and CO<sup>\*</sup> intermediates. The proximity of oxygen vacancies and Ti-H species contributes to the C-C coupling of intermediates into acetylene (C<sub>2</sub>H<sub>2</sub>) products. To the best of our knowledge, this is the first example for the photocatalytic CO<sub>2</sub> reduction into C<sub>2</sub>H<sub>2</sub> main products. The optimal hydrogenated SrTiO<sub>3</sub> has the C<sub>2</sub>H<sub>2</sub> yield of 39.0 μmol·g<sup>-1</sup> with a 76.0 % selectivity among C<sub>2</sub> products. Therefore, this work provides an approach of designing the adjacent active sites for photocatalytic CO<sub>2</sub> conversion into C<sub>2+</sub> products.

## 1. Introduction

The burning of fossil energy produces excessive carbon dioxide (CO<sub>2</sub>) emissions, resulting in an imbalance in the natural carbon cycle, gradually warming the global climate and causing environmental problems. In late years, carbon neutralization through the conversion and utilization of CO<sub>2</sub> has become the focus of consideration [1–3]. Artificial photocatalysis is a promising alternative method for converting CO<sub>2</sub> and H<sub>2</sub>O into chemicals under environmental conditions using renewable solar energy, and has received extensive attention [4–7]. Many photocatalyst materials are active to CO<sub>2</sub> reduction [8–11]. However, most of photocatalysts can only produce poor added-value products, typically such as methane or carbon monoxide [12–14]. Photocatalytic CO<sub>2</sub> reduction into C-C coupled products with a high selectivity and conversion efficiency is a grand challenge but is highly desirable for industrial applications [15,16].

Photocatalytic CO<sub>2</sub> reduction into multi-carbon (C<sub>2+</sub>) products involves multiple electron transport [17], C-C coupled steps [18,19] and requires high energy barriers [20], which determines that the process is kinetically sluggish. This requires that photocatalyst not only enables the separation and transfer of photogenerated charge carriers [21], but

also has the adjacent reaction sites for CO<sub>2</sub> activation and C-C coupling [22]. To achieve an efficient surface reaction rates and tuning selectivity into high-quantity hydrocarbons, many efforts have been devoted to the metal-cocatalyst modification combining with surface local structure fabrication to photocatalyst in CO<sub>2</sub> conversion [23]. Typically, Cu-based cocatalysts or single atoms has been widely investigated for CO<sub>2</sub> reduction to C<sub>2+</sub> products. Some C<sub>2</sub> products ethane, ethylene, and ethanol have been reported over the designed multicomponent photocatalysts [24–26]. However, to the best of our knowledge, acetylene as the main C<sub>2</sub> products have never been reported over photocatalysts for the photocatalytic CO<sub>2</sub> reduction. Acetylene, as a C-C triple-bond chemical and fuel, is an important product with extremely diverse chemistries and is used as a fuel for polymers, fuels, coatings, solvents, adhesives, and other carbon-based products [27].

For photocatalytic CO<sub>2</sub> reduction reactions, the C-C coupling process is extremely sensitive to catalyst structure [28]. Surface oxygen deficiency displays the enhanced photocatalytic CO<sub>2</sub> reduction efficiency because oxygen deficiency plays a key role in the adsorption and activation of CO<sub>2</sub> into CO<sup>\*</sup> species. [29] which is an important intermediate for the further C-C coupling. If we create a reactive center adjacent to oxygen deficiency sites for another CO<sub>2</sub> activation and conversion on

\* Corresponding author.

\*\* Corresponding author at: State Key Laboratory of Photocatalysis on Energy and Environment, College of Chemistry, Fuzhou University, Fuzhou 350106, PR China.

E-mail addresses: [t15067@fzu.edu.cn](mailto:t15067@fzu.edu.cn) (J. Shen), [z.zhang@fzu.edu.cn](mailto:z.zhang@fzu.edu.cn) (Z. Zhang).

photocatalyst surface, photo-catalyst can realize the efficient C–C coupling into C<sub>2</sub> products. [30].

Herein, we fabricated simultaneously Ti-H species and oxygen deficiency on SrTiO<sub>3</sub> by simple hydrogenation with NaBH<sub>4</sub> heating treatment. The hydrogenated SrTiO<sub>3</sub> determines the formation of C<sub>2</sub> products from the photocatalytic CO<sub>2</sub> reduction with H<sub>2</sub>O. The C<sub>2</sub>H<sub>2</sub> as main products showed a yield of up to 39.0 μmol·g<sup>-1</sup> with a 76.0 % selectivity among C<sub>2</sub> products. The oxygen deficiency induces the activation of CO<sub>2</sub> into CO\* species, while Ti-H species enables the activation of CO<sub>2</sub> into \*HCOO species. Ti-H species proximity to oxygen deficiency plays a vital role in C–C coupling into C<sub>2</sub>H<sub>2</sub> products.

## 2. Experimental

### 2.1. Chemicals and materials

Sr(NO<sub>3</sub>)<sub>2</sub> (strontium nitrate), tetrabutyl titanate, NaOH (sodium hydroxide), and ethylene glycol were purchased from Sinopharm Group. NaBH<sub>4</sub> (sodium borohydride) was purchased from Aladdin. All materials were of analytical grade and were used without further purification.

### 2.2. Synthesis of SrTiO<sub>3</sub>

In a representative synthesis, 0.01 mol of tetrabutyl titanate was dissolved in 20 mL of ethylene glycol (EG) and stirred to become a clear solution A, then 20 mL of 0.5 M Sr(NO<sub>3</sub>)<sub>2</sub> solution B was added, and finally 10 mL 5 M NaOH. After stirring for 30 min, it was transferred to a rustless steel autoclave lined with polytetrafluoroethylene and heated at 200 °C for 24 h., sonicated with water and ethanol for 10 h, centrifuged several times, and dried at 60 °C overnight.

### 2.3. Preparation of hydrogenated SrTiO<sub>3</sub> catalysts

The SrTiO<sub>3</sub> and NaBH<sub>4</sub> powders were mixed and ground in an agate mortar and then put the mixture in a porcelain boat and put it in a tube stove. Heating from room temperature to 325–400 °C at a heating velocity of 5 °C·min<sup>-1</sup> under Ar atmosphere, and then maintaining at the design temperature for 30–60 min. After natural cooling, the unreacted NaBH<sub>4</sub> was removed by simple washing with deionized water and ethanol several times, and dried at 60 °C to obtain hydrogenated SrTiO<sub>3</sub>. The ratio of SrTiO<sub>3</sub> to NaBH<sub>4</sub> was set to be 1:1, 1:2, 1:3, 1:4, 1:5 for the preparation of the hydrogenated SrTiO<sub>3</sub> (marked as HSTO-1, HSTO-2, HSTO-3, HSTO-4, and HSTO-5, respectively).

### 2.4. Photocatalyst characterization

The crystal phase of the photocatalyst was identified by XRD, Bruker D8 Advance and Ni- filtered Cu K $\alpha$  irradiation. The optical absorption capacity of the samples was characterized by UV-Vis diffuse reflectance spectroscopy (DRS, Cary-500). Transmission electron microscopy (TEM, Philips-FEI Tecnai F30 300 kW) was used to observe the size of the catalyst and its lattice fringes. We used Varian (720-ES) model ICP-AES (inductively coupled plasma atomic emission spectrometry) for detection. The hydrogen spectrum of the sample was tested on the Bruker AVANCE NEO 400 WB solid superconducting nuclear magnetic resonance spectrometer (Switzerland, Fällanden). The sample specific surface area was tested on Micromeritics 3Flex. The binding energy and surface chemical state of the samples were measured by X-ray photo-electron spectroscopy (XPS, Thermo ESCALAB 250). Shanghai Chenhua (CHI660E) electrochemical workstation was used to test the photocurrent and impedance of the samples. Test the composition of the liquid after reaction on Bruker (14.1 T/600 MHz)/AVANCE NEO 600 liquid. We used a platinum electrode as the counter electrode and an Ag/AgCl electrode as the reference electrode for the photocurrent measurement (3 M KCl). The catalyst was impregnated onto FTO glass to create the working electrode. The three-electrode system was measured in Na<sub>2</sub>SO<sub>4</sub>

(0.2 m) electrolyte. Nyquist plots are measured at 0.5 × 10<sup>5</sup> to 1.5 × 10<sup>5</sup> Hz intervals. Detection of defect sites in catalyst was carried out by EPR (EPR, Bruker A-300). The EPR test condition is 110 K, under CO<sub>2</sub> atmosphere, 254 nm point light source illumination for 0–20 min. The reaction intermediates were investigated by VERTX 70v FT-IR spectrometer.

### 2.5. Photocatalytic activity

Atmospheric pressure research on the photocatalytic reduction of CO<sub>2</sub> was conducted in a 50 mL quartz batch reactor. The illuminant was four ultraviolet lamps with a central wavelength of 254 nm (PHILIPS TUV 8 W G8 T5) with the light intensity of 1.6 mW·cm<sup>-2</sup>, which were placed on both sides of the reactor in parallel. In typical photocatalysis experiments, 10 mg of photocatalyst powders were loaded in the reactor. The reactor was evacuated with a vacuum pump and then filled with pure gaseous carbon dioxide. Repeat the same operation 7–10 times. In the last operation, the reactor was filled with high pure CO<sub>2</sub> and 5 mL of deionized water, and the sampling port of the reactor was sealed with a rubber stopper and a sealing tape. After 6 h ultraviolet light irradiation for the photocatalytic reaction. 0.5 mL of gas was withdrawn from the reactor for subsequent gas concentration analysis. CO, methane acetylene, ethylene, and ethane were detected using a process gas chromatograph (GC-7890A) equipped with a flame ionization detector (FID). H<sub>2</sub> was identified by Shimadzu GC-2014 C equipped with TCD and 5 Å molecular sieve column.

## 3. Results and discussion

### 3.1. Structure and chemical state of SrTiO<sub>3</sub>

The crystallographic structure and component phases of HSTO samples were determined by XRD. As shown in Fig. 1a, all the diffraction apexes were consistent with the characteristic diffraction peaks of STO (JCPDS35–0734). The XRD pattern intensity of HSTO had no significant change and no diffraction peaks of impurities were observed. This indicated that the hydrogenation through NaBH<sub>4</sub> treatment did not alter the crystal structure of STO. TEM (Fig. 1b) image displayed that the edges of STO grains are clear for the high crystallinity of samples. However, the apparent cavity-like structures were randomly distributed on the surface of STO grain. The hydrogenation had no effect on the grain structure of STO (Fig. 1d). According to the HRTEM images (Fig. 1c and 1e), the distinct lattice fringe spacing of 0.275 nm was observed both STO and HSTO samples, which corresponds to the (110) plane of STO. The N<sub>2</sub> isotherm adsorption/desorption measurements (Fig. S1) confirmed that both pure STO and HSTO exhibited the characteristics of porous materials. The specific surface area of STO and HSTO-4 were 59.2 m<sup>2</sup>·g<sup>-1</sup> and 57.0 m<sup>2</sup>·g<sup>-1</sup>, respectively. This suggested that the hydrogenation by NaBH<sub>4</sub> treatment had a negligible influence on the morphological structure of STO. In addition, the atomic ratio of Sr and Ti in the sample before and after treatment was determined to be 1:1 by inductively coupled plasma emission spectroscopy (ICP-AES), so it can be concluded that the total stoichiometry of Sr and Ti before and after hydrogenation treatment remained unchanged.

The chemical states of STO and HSTO-4 were investigated using XPS (Fig. 2). Charge calibration was performed using C1 (284.8 eV) of the contaminated carbon. Sr 3d XPS had no significant differences between STO and HSTO-4 samples (Fig. 2a). However, HSTO-4 produced a small peak of Ti<sup>3+</sup> states in Ti 2p XPS [31], besides the main peak of Ti<sup>4+</sup> at 458.29 eV [32,33] had a positive shift by 0.1 eV as compared with the pristine STO (Fig. 2b). This demonstrated that NaBH<sub>4</sub> hydrogenation made a reduction of partial Ti<sup>4+</sup> to Ti<sup>3+</sup> states. The fitted O1s XPS was shown in Fig. 2c. There were two different states of oxygen on STO. The binding energies at 529.4 eV and 531.2 eV belonged to lattice oxygen and surface hydroxyl of STO [34], respectively. The O1s binding energy of HSTO-4 showed a visible shift to higher energy. Moreover, the surface

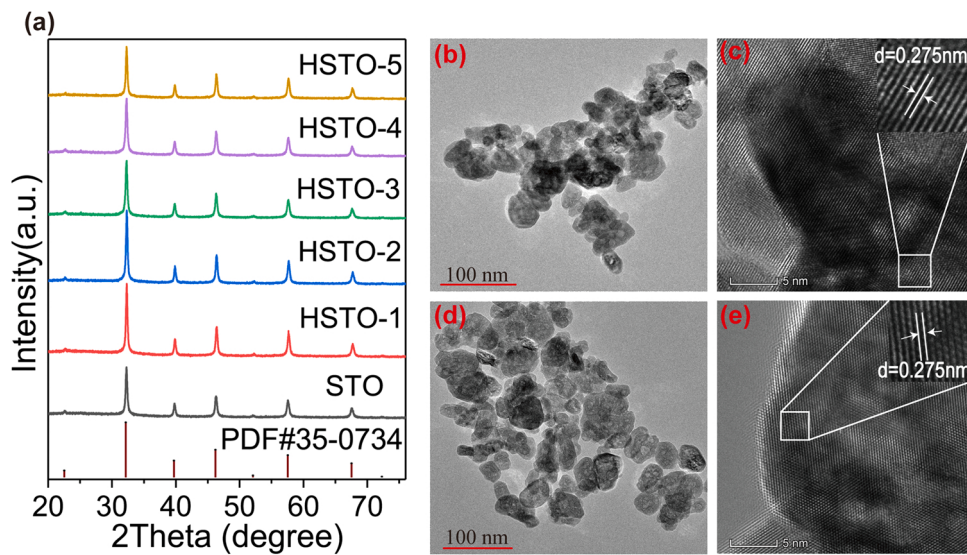


Fig. 1. (a) XRD patterns of STO treated with different  $\text{NaBH}_4$  additions, (b) TEM and (c) HRTEM images of STO, (d) TEM and (e) HRTEM images of HSTO-4.

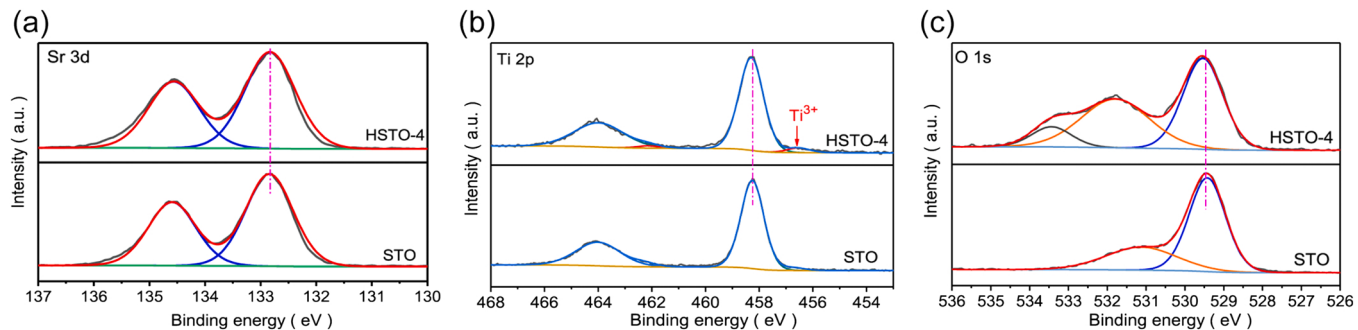


Fig. 2. XPS spectra of STO and HSTO-4, (a) Sr3d, (b) Ti2p, and (c) O1s.

hydroxyl deriving from the oxygen defects was significantly enhanced on HSTO-4. With the increase of reaction time and temperature, Ti and O gradually transfer to high binding energy. All of element XPS had a similar shift to higher binding energy. This demonstrated a characteristic shift of Fermi level for HSTO-4 [35]. The oxygen deficiency and reduction state of  $\text{SrTiO}_3$  enhance the equilibrium electron density, thus

promoting the increase of Fermi level. This confirmed the  $\text{NaBH}_4$  hydrogenation of STO to form large number of oxygen defects.

The hydrogenated species on HSTO was identified by the solid-state  $^1\text{H}$  NMR spectrum (Fig. 3a). Several chemical shift ( $\delta$ ) peaks were observed on STO and HSTO-4 at  $\delta = 0\text{--}1$  ppm, and  $\delta = 3\text{--}5$  ppm. The signal peak at  $\delta = 0\text{--}1$  ppm can be attributed to surface OH group [36],

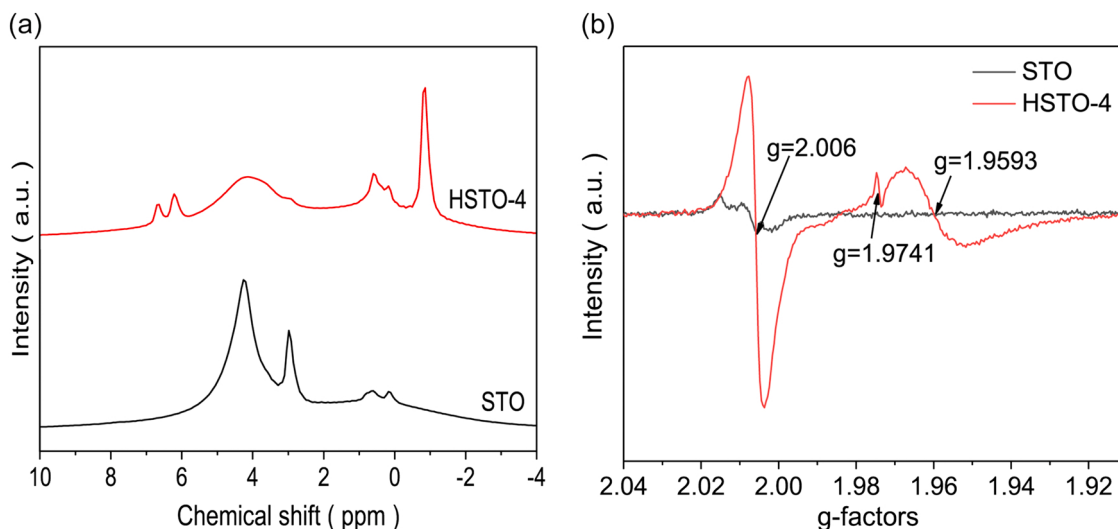


Fig. 3. (a) The solid-state  $^1\text{H}$  NMR spectra. (b) The EPR spectra at 110 K temperature under vacuum.

while the signal at  $\delta = 3\text{--}5$  ppm can be assigned to the absorbed  $\text{H}_2\text{O}$  in STO [37]. The absorbed  $\text{H}_2\text{O}$  signal peak in HSTO-4 was remarkably decreased. However, the new main peak centered at the chemical shift of  $-0.87$  ppm was noticed in HSTO-4. This indicated that there was a new chemical environment for hydrogen species. The hydrogen species can be allocated to Ti-H species [38]. Therefore,  $\text{NaBH}_4$  hydrogenation resulted in the local structure change of HSTO surface and Ti-H species formation. The low-temperature electron paramagnetic resonance (EPR) spectroscopy at 110 K further elucidated defects in samples, as shown in Fig. 3b. The signals at  $g = 1.9593$  and  $1.9741$  were assigned to the paramagnetic  $\text{Ti}^{3+}$  species generated on HSTO-4, and the signal at  $g = 2.006$  of the oxygen vacancies was greatly enhanced on HSTO-4 [39]. This confirmed the abundant oxygen vacancies and  $\text{Ti}^{3+}$  species in HSTO-4. According to UV-Vis diffuse reflectance spectra (Fig. S2), the absorption band of STO was about 390 nm. HSTO extended the absorption side gradually to the visible light region of about 410 nm due to the presence of  $\text{V}_\text{O}$  and  $\text{Ti}^{3+}$  species in HSTO.

### 3.2. Photocatalytic reduction of $\text{CO}_2$ to $\text{C}_2$ products

The photocatalytic performance of  $\text{CO}_2$  photocatalytic reduction was investigated in a batch reactor under 8 W 254 nm ultraviolet illumination. First, the effect of the hydrogenation of STO on the photocatalytic reduction of  $\text{CO}_2$  to  $\text{C}_2$  was studied, as shown in Fig. 4. The pristine STO can produce a few of  $\text{CO}$  ( $4.34 \mu\text{mol}\cdot\text{g}^{-1}$ ) and  $\text{CH}_4$  ( $2.77 \mu\text{mol}\cdot\text{g}^{-1}$ ) products, but have no activity to reduce  $\text{CO}_2$  to  $\text{C}_2$  in the photocatalytic reaction. Upon the hydrogenation of STO, the HSTO samples displayed unexpectedly the reduction of  $\text{CO}_2$  to mainly  $\text{C}_2$  hydrocarbons including  $\text{C}_2\text{H}_2$ ,  $\text{C}_2\text{H}_4$  and  $\text{C}_2\text{H}_6$ , besides the improvement of  $\text{CO}$  and  $\text{CH}_4$  formation. The product yields were influenced by the hydrogenation degree with increasing  $\text{NaBH}_4$  treatment. Among various hydrogenated samples, HSTO-4 processed the highest activity for  $\text{CO}_2$  photocatalytic reduction performance. As a result, the products  $\text{C}_2\text{H}_2$  showed a yield of up to  $38.98 \mu\text{mol}\cdot\text{g}^{-1}$ , along with  $\text{C}_2\text{H}_4$  ( $5.69 \mu\text{mol}\cdot\text{g}^{-1}$ ),  $\text{C}_2\text{H}_6$  ( $6.63 \mu\text{mol}\cdot\text{g}^{-1}$ ),  $\text{CO}$  ( $19.96 \mu\text{mol}\cdot\text{g}^{-1}$ ) and  $\text{CH}_4$  ( $11.75 \mu\text{mol}\cdot\text{g}^{-1}$ ) products. Obviously,  $\text{C}_2$  hydrocarbons, especially  $\text{C}_2\text{H}_2$ , were the main products of  $\text{CO}_2$  reduction over HSTO-4. Among  $\text{CO}_2$  reduction products,  $\text{C}_2$  product selectivity reached 76.4 %, and  $\text{C}_2\text{H}_2$  selectivity was 76.0 % among  $\text{C}_2$  products. No other carbon-based compounds (such as  $\text{CH}_3\text{OH}$ ,  $\text{HCOOH}$ ,  $\text{HCHO}$ , etc.) were detected in the gaseous products by gas chromatography. In addition, using  $^1\text{H}$  NMR spectroscopy to detect possible products in the liquid phase after the reaction, only a strong signal ( $\delta = 4.79$ ) pointing to  $\text{D}_2\text{O}$  was noticed in the  $^1\text{H}$  NMR spectrum (Fig. S3), which further confirmed that no liquid products such as  $\text{CH}_3\text{OH}$  or  $\text{HCOOH}$  were produced. At the same time, we checked whether the reaction products contained oxidation products through repeated experiments. Unfortunately, no oxidation products such as  $\text{O}_2$ ,  $\text{H}_2\text{O}_2$  products were detected in our reaction system. In order to further confirm whether oxidation intermediates were produced in the reaction process, we used EPR to detect hydroxyl radical intermediates to

confirm the ability of HSTO-4 photocatalyst for  $\text{H}_2\text{O}$  oxidation (Fig. S4). The signals of hydroxyl radicals were remarkably produced in EPR spectra, indicating that HSTO-4 photocatalyst enables  $\text{H}_2\text{O}$  oxidation into oxidation products in the reaction. The reason may be that the oxidation products such as  $\text{O}_2$  were dissolved in water or adsorbed on photocatalyst surface, so that a small amount of  $\text{O}_2$  products in the gas phase can't be detected by GC.

Control experiments showed that in the absence of  $\text{CO}_2$  gas or catalyst, almost no  $\text{C}_2$  products were generated in the reaction system. This proved that all  $\text{C}_2$  products were derived from the photocatalytic  $\text{CO}_2$  reduction reaction. In addition, the isotope labeling experiment used  $^{13}\text{CO}_2$  as the reactant, and other reaction conditions remained unchanged. The results indicated that the products  $\text{CO}$ ,  $\text{C}_2\text{H}_6$ ,  $\text{CH}_4$  and  $\text{C}_2\text{H}_2$  were all derived from photocatalytic  $^{13}\text{CO}_2$  reduction (Fig. 5). Due to the low yield of  $^{13}\text{C}_2\text{H}_4$  and the overlap of  $m/z$  peak of  $^{13}\text{C}_2\text{H}_4$  with the fragments of  $^{13}\text{C}_2\text{H}_6$ , the individual mass spectra of  $^{13}\text{C}_2\text{H}_4$  were not specifically pointed out. The calcination time and temperature of  $\text{NaBH}_4$  after STO treatment were optimized, and its effect on photocatalytic activity was shown in the Fig. S5. Obviously, the optimal calcination temperature of  $\text{NaBH}_4$  treatment is  $375^\circ\text{C}$  and the calcination time is 1 h. In addition to  $\text{C}_1$  and  $\text{C}_2$  products, there were a large amount of  $\text{H}_2$  products in the reaction system (Fig. S6). The yield of  $\text{H}_2$  was better than that of carbon matrix products, because STO was one of the good catalysts for water splitting into  $\text{H}_2$  [40]. It was worth noting that the used catalyst was characterized XRD and  $^1\text{H}$  NMR. XRD pattern showed that the crystal phase of catalysts was not altered after photocatalytic reaction (Fig. S7a).  $^1\text{H}$  NMR spectra (Fig. S7b) showed that the intensity of Ti-H species at  $\delta = -0.87$  ppm significantly decreased after the reaction. Obviously, Ti-H species was involved in the reaction, which may be one of the reasons for catalyst deactivation with prolonging reaction.

As everyone knows that  $\text{NaBH}_4$  can generate  $\text{V}_\text{O}$  on the surface of the sample. To determine whether the photocatalytic  $\text{C}_2$  formation was related to the B doping or oxygen vacancy defects on HSTO samples from  $\text{NaBH}_4$  treatment, the reference samples of  $\text{B}_2\text{O}_3$  or  $\text{H}_2$  heating treatment to induce B doping or oxygen vacancy defects on STO were prepared respectively. It was worth noting that  $\text{H}_2$  treated samples also produced trace amounts of Ti-H (Fig. S8), as compared with the Ti-H content produced by  $\text{NaBH}_4$  treatment. Due to the high energy barrier requirement for  $\text{H}_2$  molecule dissociation into  $\text{H}$  atom, while the low energy barrier requirement for releasing active hydrogen in  $\text{NaBH}_4$ ,  $\text{NaBH}_4$  treatment was favorable to produce the Ti-H species on  $\text{SrTiO}_3$  surface under the similar calcination temperature. The photocatalytic activity showed that both B doping and oxygen vacancy defects of STO can hardly reduce  $\text{CO}_2$  to  $\text{C}_2\text{H}_2$  (Fig. S9). Furthermore, the intensity of the oxygen vacancies in EPR of various HSTO samples (Fig. S10) is inconsistent with the order of their photocatalytic activities of  $\text{C}_2$  formation. Thus, the possible B doping or only oxygen vacancy defects cannot achieve  $\text{C}_2\text{H}_2$  formation on STO.  $\text{Ti}^{3+}$  or Ti-H species maybe play a vital role in  $\text{C}_2$  formation on HSTO samples.

### 3.3. Mechanism exploration

The photogenerated electron/hole pair separation ability of HSTO samples were investigated by photoelectrochemical measurements. Compared with STO, the photocurrent of HSTO-4 was significantly enhanced under UV light (Fig. 6a). This implies that HSTO samples can improve the separation efficiency of photo-induced carriers. The electrochemical impedance spectroscopy (EIS) Nyquist plot (Fig. 6b) showed that the arc radius of HSTO-4 was significantly smaller than that of STO. This confirms the dramatic photogenerated electron/hole separation capability of HSTO-4, which is favorable for the transfer of interfacial charges to the surface and the occurrence of redox reactions. The improvement of electron/hole separation ability of HSTO samples was attribute to the oxygen vacancies and  $\text{Ti}^{3+}$  formation on HSTO samples. Thus,  $\text{CO}$  and  $\text{CH}_4$  yields were enhanced over HSTO samples as compared with STO.

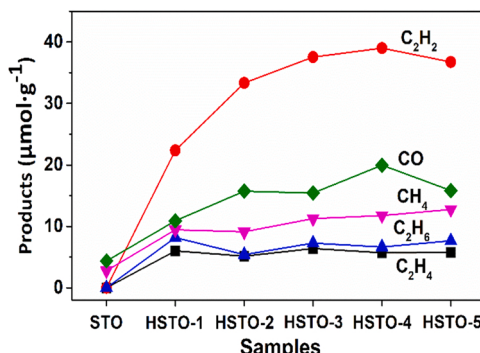


Fig. 4. Activity plots of various hydrogenated samples for 6 h reaction.

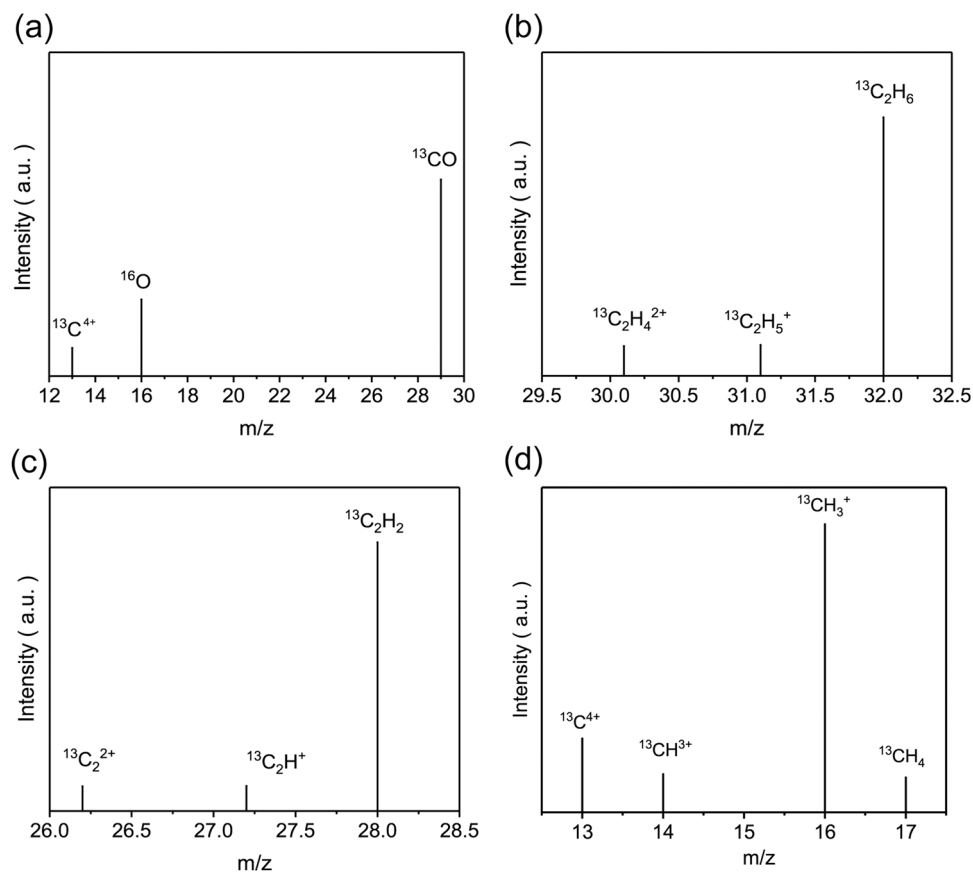


Fig. 5. Mass-spectrogram of HSTO-4 (a)  $^{13}\text{CO}$ , (b)  $^{13}\text{C}_2\text{H}_6$ ,  $^{13}\text{C}_2\text{H}_4$  and (c)  $^{13}\text{C}_2\text{H}_2$  (d)  $^{13}\text{CH}_4$ .

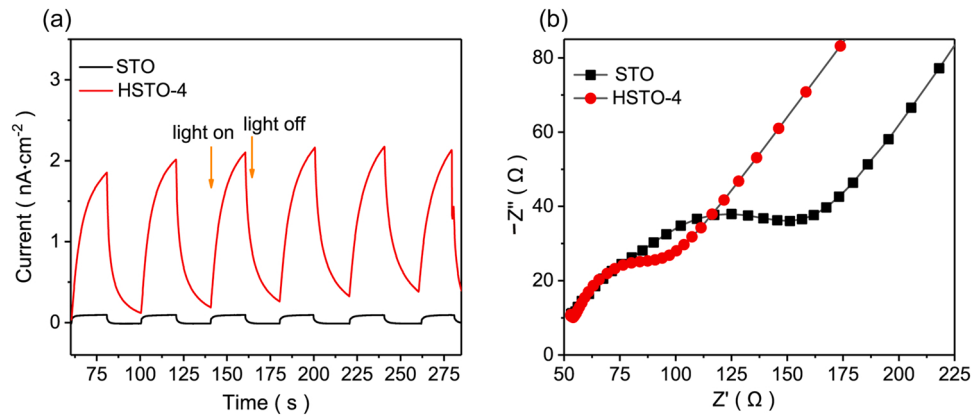


Fig. 6. (a) Electrochemical photocurrent and (b) electrochemical impedance spectra.

However, the improvement of electron/hole separation was difficult to explain the selectivity to  $\text{C}_2+$  compound formation on HSTO samples. Compared with the surface structure of parent STO, the formed defect sites and Ti-H species on HSTO-4 should be accounted for the selectivity of  $\text{C}_2\text{H}_2$  formation. To understand the interaction of active sites with  $\text{CO}_2$  activation and conversion, we used *in situ* Fourier transform infrared spectroscopy (FTIR) to monitor  $\text{CO}_2$  absorption and intermediates on STO and HSTO-4. As shown in Fig. 7a,  $\text{CO}_2$  was adsorbed on the nude STO surface mainly in the form of carboxylate ( $\text{CO}_2^-$ ,  $1650\text{ cm}^{-1}$ ). Under light irradiation (Fig. 7b), only the infrared peaks of  $^*\text{COOH}$  ( $1593\text{ cm}^{-1}$ ) and C-H ( $1338\text{ cm}^{-1}$ ) group appeared on STO. The production of  $^*\text{COOH}$  was an important intermediate to further couple with proton-electron pairs to generate CO and  $\text{CH}_4$  products. However, the

quite different adsorbed species of  $\text{CO}_2$  were formed on the surface of HSTO-4, as shown in Fig. 7c.  $\text{CO}^*$  ( $2075\text{ cm}^{-1}$ ), and  $\text{HCOO}^-$  ( $1386\text{ cm}^{-1}$ ) can be identified for  $\text{CO}_2$  absorption on HSTO-4, which can arise from the interaction of  $\text{CO}_2$  with oxygen vacancy and Ti-H active sites, respectively. Under light irradiation, a series of intermediates and products, including C-H bond of alkynes ( $3126$ ,  $2337\text{ cm}^{-1}$ ) [41], C-H of olefins ( $3127\text{ cm}^{-1}$ ), C-H of alkanes ( $2926\text{ cm}^{-1}$ ) [42], and  $\text{CO}_2$  ( $1688\text{ cm}^{-1}$ ) [43] were formed upon irradiation and enhanced with increasing irradiation time (Fig. 7d), while  $\text{CO}^*$  ( $2075\text{ cm}^{-1}$ ) intermediates disappeared upon irradiation and  $\text{HCOO}^-$  ( $1386\text{ cm}^{-1}$ ) was a negative growth with increasing irradiation time. This well demonstrates that  $\text{CO}^*$  and  $\text{HCOO}^-$  are important intermediates for the conversion into  $\text{C}_2+$  products.

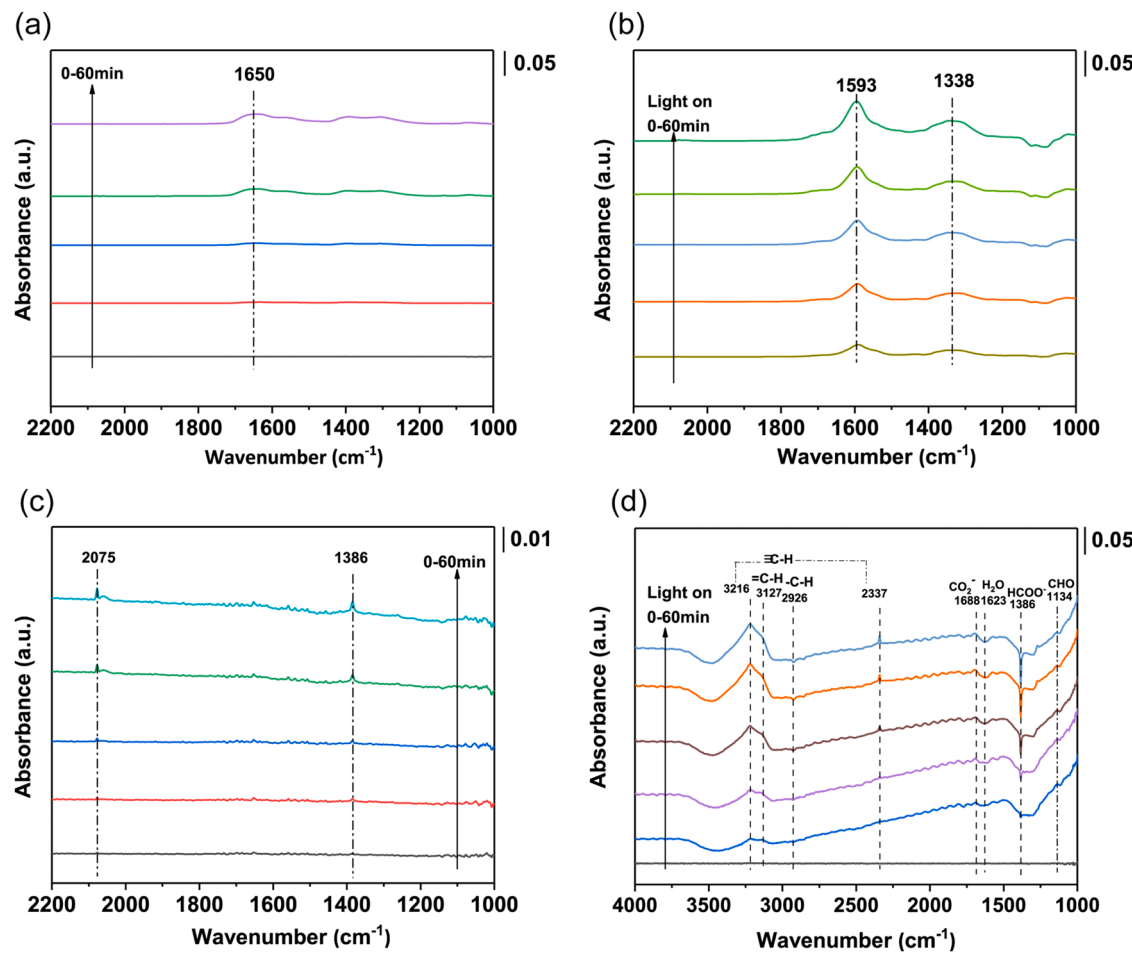


Fig. 7. *in situ* FTIR of CO<sub>2</sub> absorption and conversion (a) on STO in darkness, (b) on STO with light, (c) on HSTO-4 in darkness and (d) on HSTO-4 with light.

Based on these observations, the photocatalytic CO<sub>2</sub> reduction pathway on HSTO-4 was proposed in Fig. 8. The HSTO-4 catalyst had two adjacent active sites of V<sub>O</sub> and Ti-H. Under dark conditions, CO<sub>2</sub> was adsorbed at V<sub>O</sub> site in the form of oxygen coordination. Thus, the oxygen of CO<sub>2</sub> occupied the V<sub>O</sub> to dissociate to the adsorbed CO\* species [44].

This is consistent with the observation of CO\* in the *in situ* FTIR spectra. This results in that the V<sub>O</sub> signal is weakened in the presence of CO<sub>2</sub> in EPR spectra as compared with the pure HSTO-4 (Fig. S11). However, another CO<sub>2</sub> was carbon-coordinated to negatively charged H of Ti-H site to form the adsorbed \*HCOO<sup>-</sup> intermediates. Under the light

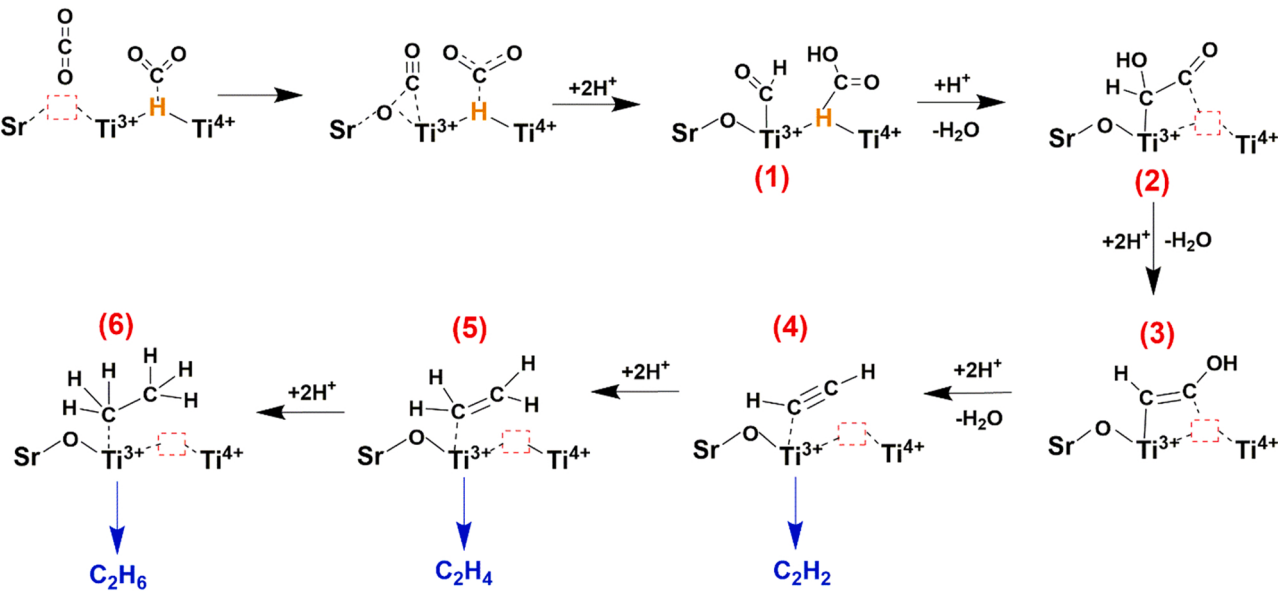


Fig. 8. Mechanism of CO<sub>2</sub> reduction into C<sub>2</sub> products over HSTO-4.

excitation of HSTO-4, the adsorbed  $\text{CO}^*$  species underwent proton coupled electron transfer into  $\text{CHO}^*$  intermediates, while the adsorbed  $^*\text{HCOO}^-$  was combined with proton into  $^*\text{HCOOH}$  intermediates. The adjacent  $\text{CHO}^*$  and  $^*\text{HCOOH}$  intermediates on HSTO-4 involved proton coupled electron transfer, dehydration and C-C coupling to form carbon–carbon bond intermediates (2) on HSTO-4, which further proceeded the proton coupled electron transfer and dehydration into carbon–carbon double bond intermediates (3) on HSTO-4. The carbon–carbon double bond intermediates (3) went ahead with the proton coupled electron transfer and dehydration processes to form adsorbed  $\text{C}_2\text{H}_2$  (4) on HSTO-4, which can be desorbed into  $\text{C}_2\text{H}_2$  products. The adsorbed  $\text{C}_2\text{H}_2$  can be converted into the adsorbed  $\text{C}_2\text{H}_4$  (5) and  $\text{C}_2\text{H}_6$  (6) through the further proton coupled electron transfer and finally released into the corresponding  $\text{C}_2$  products. Due to the shortest reaction path and the least proton coupled electron transfer,  $\text{C}_2\text{H}_2$  was kinetically beneficial to form as main products, as compared with  $\text{C}_2\text{H}_4$  and  $\text{C}_2\text{H}_6$ .

#### 4. Conclusion

We developed the  $\text{NaBH}_4$  heating treatment approach for the simultaneous creation of Ti-H species and  $\text{V}_0$  on the surface of  $\text{SrTiO}_3$  photocatalyst. The synergistic effect of the proximity of Ti-H species and oxygen vacancy promoted the coupling of  $\text{CO}^*$  and  $\text{HCOO}^-$  intermediates into  $\text{C}_2$  products during photocatalytic  $\text{CO}_2$  reduction.  $\text{C}_2\text{H}_2$  as the main products with a yield of  $38.98 \mu\text{mol}\cdot\text{g}^{-1}$  and selectivity of 76.0 % among  $\text{C}_2$  products was achieved on the modified  $\text{SrTiO}_3$  photocatalyst. we conclude that this work provides a design idea of simple photocatalysts for the conversion of  $\text{CO}_2$  into  $\text{C}_{2+}$  products.

#### CRediT authorship contribution statement

**Haiying Xu:** Data curation, Sample characterization, Writing original draft. **Zhaoliang Wang:** Sample characterization, Writing original draft. **Hehua Liao:** Data curation, Sample characterization. **Dongmiao Li:** Data analysis, Writing original draft. **Jinni Shen:** Writing - review & editing, Supervision. **Jinlin Long:** Writing - review & editing. **Wenxin Dai:** Writing - review & editing. **Xuxu Wang:** Writing - review & editing, Supervision. **Zizhong Zhang:** Project administration, Funding acquisition, Supervision, Conceptualization, Writing - review & editing.

#### Declaration of Competing Interest

The authors declare that they have no known competing financial interests or personal relationships that could have appeared to influence the work reported in this paper.

#### Data availability

The data that has been used is confidential.

#### Acknowledgements

This work is financially supported by the National Natural Science Foundation of China (Grants No. 21972020), and Natural Science Foundation of Fujian Province of PR China (2020L3003).

#### Appendix A. Supporting information

Supplementary data associated with this article can be found in the online version at [doi:10.1016/j.apcatb.2023.122935](https://doi.org/10.1016/j.apcatb.2023.122935).

#### References

- [1] X. Li, J. Yu, M. Jaroniec, X. Chen, Cocatalysts for selective photoreduction of  $\text{CO}_2$  into solar fuels, *Chem. Rev.* 119 (2019) 3962–4179, <https://doi.org/10.1021/acs.chemrev.8b00400>.
- [2] L. Wang, L. Wang, J. Zhang, X. Liu, H. Wang, W. Zhang, Q. Yang, J. Ma, X. Dong, S. J. Yoo, J.-G. Kim, X. Meng, F.-S. Xiao, Selective hydrogenation of  $\text{CO}_2$  to ethanol over cobalt, *Catal. Angew. Chem. Int. Ed.* 57 (2018) 6104–6108, <https://doi.org/10.1002/anie.201800729>.
- [3] L. Chen, G. Msigwa, M. Yang, A.I. Osman, S. Fawzy, D.W. Rooney, P.-S. Yap, Strategies to achieve a carbon neutral society: a review, *Environ. Chem. Lett.* 20 (2022) 2277–2310, <https://doi.org/10.1007/s10311-022-01435-8>.
- [4] M. Lin, H. Chen, Z. Zhang, X. Wang, Engineering interface structure for heterojunction photocatalysts, *Phys. Chem. Chem. Phys.* 25 (2023) 4388–4407, <https://doi.org/10.1039/d2cp05281>.
- [5] A. Li, Q. Cao, G. Zhou, B.V.K.J. Schmidt, W. Zhu, X. Yuan, H. Huo, J. Gong, M. Antonietti, Three-phase photocatalysis for the enhanced selectivity and activity of  $\text{CO}_2$  reduction on a hydrophobic surface, *Angew. Chem. Int. Ed.* 58 (2019) 14549–14555, <https://doi.org/10.1002/anie.201908058>.
- [6] Y. Chai, Y. Chen, J. Shen, M. Ni, B. Wang, D. Li, Z. Zhang, X. Wang, Distortion of the coordination structure and high symmetry of the crystal structure in  $\text{In}_x\text{Sn}_8$  microflowers for enhancing visible-light photocatalytic  $\text{CO}_2$  reduction, *ACS Catal.* 11 (2021) 11029–11039, <https://doi.org/10.1021/acscatal.1c02937>.
- [7] Y. Wang, X. Shang, J. Shen, Z. Zhang, D. Wang, J. Lin, J.C.S. Wu, X. Fu, X. Wang, C. Li, Direct and indirect Z-scheme heterostructure-coupled photosystem enabling cooperation of  $\text{CO}_2$  reduction and  $\text{H}_2\text{O}$  oxidation, *Nat. Commun.* 11 (2020) 3043, <https://doi.org/10.1038/s41467-020-16742-3>.
- [8] M. Gao, J. Yang, T. Sun, Z. Zhang, D. Zhang, H. Huang, H. Lin, Y. Fang, X. Wang, Persian buttercup-like  $\text{BiOBr}_x\text{Cl}_{1-x}$  solid solution for photocatalytic overall  $\text{CO}_2$  reduction to  $\text{CO}$  and  $\text{O}_2$ , *Appl. Catal. B Environ.* 243 (2019) 734–740, <https://doi.org/10.1016/j.apcatb.2018.11.020>.
- [9] L. Lin, P. Lin, J. Song, Z. Zhang, X. Wang, W. Su, Boosting the photocatalytic activity and stability of  $\text{Cu}_2\text{O}$  for  $\text{CO}_2$  conversion by  $\text{LaTiO}_2\text{N}$ , *J. Colloid Interface Sci.* 630 (2023) 352–362, <https://doi.org/10.1016/j.jcis.2022.10.026>.
- [10] Y. Liu, B. Wang, D. Li, J. Shen, Z. Zhang, X. Wang, Fabrication of 2H/3C-SiC heterophase junction nanocages for enhancing photocatalytic  $\text{CO}_2$  reduction, *J. Colloid Interface Sci.* 622 (2022) 31–39, <https://doi.org/10.1016/j.jcis.2022.04.111>.
- [11] M. Ni, L. Wang, Y. Chai, B. Wang, D. Li, J. Shen, Z. Zhang, X. Wang, Multimetal tantalate  $\text{CsBi}_2\text{TaO}_6$  for photocatalytic conversion of  $\text{CO}_2$  with  $\text{H}_2\text{O}$  into  $\text{CH}_4$  and  $\text{O}_2$ , *Appl. Surf. Sci.* 588 (2022), 152933, <https://doi.org/10.1016/j.apsusc.2022.152933>.
- [12] N. Li, Y. Tu, K. Wang, D. Huang, Q. Shen, W. Chen, J. Zhou, Q. Ma, M. Liu, Construction of a Photo-thermal-magnetic coupling reaction system for enhanced  $\text{CO}_2$  reduction to  $\text{CH}_4$ , *Chem. Eng. J.* 421 (2021), 129940, <https://doi.org/10.1016/j.cej.2021.129940>.
- [13] Y. Wang, Q. Zhou, Y. Zhu, D. Xu, High efficiency reduction of  $\text{CO}_2$  to  $\text{CO}$  and  $\text{CH}_4$  via photothermal synergistic catalysis of lead-free perovskite  $\text{Cs}_3\text{Sb}_2\text{I}_9$ , *Appl. Catal. B Environ.* 294 (2021), 120236, <https://doi.org/10.1016/j.apcatb.2021.120236>.
- [14] Y.-X. Pan, Y. You, S. Xin, Y. Li, G. Fu, Z. Cui, Y.-L. Men, F.-F. Cao, S.-H. Yu, J. B. Goodenough, Photocatalytic  $\text{CO}_2$  reduction by carbon-coated indium-oxide nanobelts, *J. Am. Chem. Soc.* 139 (2017) 4123–4129, <https://doi.org/10.1021/jacs.7b00266>.
- [15] G.H. Han, J. Bang, G. Park, S. Choe, Y.J. Jang, H.W. Jang, S.Y. Kim, S.H. Ahn, Recent advances in electrochemical, photochemical, and photoelectrochemical reduction of  $\text{CO}_2$  to  $\text{C}_{2+}$  products, *Small* (2023), 2205765, <https://doi.org/10.1002/smll.202205765>.
- [16] L. Li, H. Guo, G. Yao, C. Hu, C. Liu, Z. Tian, B. Li, Q. Zhang, L. Chen, Visible/infrared light-driven high-efficiency  $\text{CO}_2$  conversion into ethane based on a B-Co synergistic catalyst, *J. Mater. Chem. A.* 8 (2020) 22327–22334, <https://doi.org/10.1039/D0TA05821A>.
- [17] C. Du, X. Wang, W. Chen, S. Feng, J. Wen, Y.A. Wu,  $\text{CO}_2$  transformation to multicarbon products by photocatalysis and electrocatalysis, *Mater. Today Adv.* 6 (2020), 100071, <https://doi.org/10.1016/j.mtadv.2020.100071>.
- [18] W. Wang, C. Deng, S. Xie, Y. Li, W. Zhang, H. Sheng, C. Chen, J. Zhao, Photocatalytic C-C coupling from carbon dioxide reduction on copper oxide with mixed-valence Copper(I)/Copper(II), *J. Am. Chem. Soc.* 143 (2021) 2984–2993, <https://doi.org/10.1021/jacs.1c00206>.
- [19] S. Yu, A.J. Wilson, J. Heo, P.K. Jain, Plasmonic control of multi-electron transfer and C-C coupling in visible-light-driven  $\text{CO}_2$  reduction on Au nanoparticles, *Nano Lett.* 18 (2018) 2189–2194, <https://doi.org/10.1021/acs.nanolett.7b05410>.
- [20] K. Li, B. Peng, T. Peng, Recent advances in heterogeneous photocatalytic  $\text{CO}_2$  conversion to solar fuels, *ACS Catal.* 6 (2016) 7485–7527, <https://doi.org/10.1021/acscatal.6b02089>.
- [21] N. Li, B. Wang, Y. Si, F. Xue, J. Zhou, Y. Lu, M. Liu, Toward high-value hydrocarbon generation by photocatalytic reduction of  $\text{CO}_2$  in water vapor, *ACS Catal.* 9 (2019) 5590–5602, <https://doi.org/10.1021/acscatal.9b00223>.
- [22] G. Jia, M. Sun, Y. Wang, Y. Shi, L. Zhang, X. Cui, B. Huang, J.C. Yu, Asymmetric coupled dual-atom sites for selective photoreduction of carbon dioxide to acetic acid, *Adv. Funct. Mater.* 32 (2022), 2206817, <https://doi.org/10.1002/adfm.202206817>.
- [23] H. Ou, G. Li, W. Ren, B. Pan, G. Luo, Z. Hu, D. Wang, Y. Li, Atomically dispersed Au-assisted C-C coupling on red phosphorus for  $\text{CO}_2$  photoreduction to  $\text{C}_2\text{H}_6$ , *J. Am. Chem. Soc.* 144 (2022) 22075–22082, <https://doi.org/10.1021/jacs.2c09424>.

[24] K. Adachi, K. Ohta, T. Mizuno, Photocatalytic reduction of carbon dioxide to hydrocarbon using copper-loaded titanium dioxide, *Sol. Energy* 53 (1994) 187–190, [https://doi.org/10.1016/0038-092X\(94\)90480-4](https://doi.org/10.1016/0038-092X(94)90480-4).

[25] S. Sorcar, Y. Hwang, J. Lee, H. Kim, K.M. Grimes, C.A. Grimes, J.-W. Jung, C.-H. Cho, T. Majima, M.R. Hoffmann, S.-I. In, CO<sub>2</sub>, water, and sunlight to hydrocarbon fuels: a sustained sunlight to fuel (Joule-to-Joule) photoconversion efficiency of 1%, *Energy Environ. Sci.* 12 (2019) 2685–2696, <https://doi.org/10.1039/C9EE00734B>.

[26] B. Zhao, Y. Liu, Z. Zhu, H. Guo, X. Ma, Highly selective conversion of CO<sub>2</sub> into ethanol on Cu/ZnO/Al<sub>2</sub>O<sub>3</sub> catalyst with the assistance of plasma, *J. CO<sub>2</sub> Util.* 24 (2018) 34–39, <https://doi.org/10.1016/j.jcou.2017.10.013>.

[27] X. Huang, S. Li, Solubility of acetylene in alcohols and ketones, *J. Chem. Eng. Data* 63 (2018) 2127–2134, <https://doi.org/10.1021/acs.jcd.8b00126>.

[28] N.-N. Vu, S. Kaliaguine, T.-O. Do, Critical aspects and recent advances in structural engineering of photocatalysts for sunlight-driven photocatalytic reduction of CO<sub>2</sub> into fuels, *Adv. Funct. Mater.* 29 (2019), 1901825, <https://doi.org/10.1002/adfm.201901825>.

[29] H. Shen, T. Ouyang, J. Guo, M. Mu, X. Yin, A perspective LDHs/Ti<sub>3</sub>C<sub>2</sub>O<sub>2</sub> design by DFT calculation for photocatalytic reduction of CO<sub>2</sub> to C<sub>2</sub> organics, *Appl. Surf. Sci.* 609 (2023), 155445, <https://doi.org/10.1016/j.apsusc.2022.155445>.

[30] C. Yang, C. Pei, R. Luo, S. Liu, Y. Wang, Z. Wang, Z.-J. Zhao, J. Gong, Strong electronic oxide–support interaction over In<sub>2</sub>O<sub>3</sub>/ZrO<sub>2</sub> for highly selective CO<sub>2</sub> hydrogenation to methanol, *J. Am. Chem. Soc.* 142 (2020) 19523–19531, <https://doi.org/10.1021/jacs.0c07195>.

[31] B. Psiuk, J. Szade, K. Szot, SrTiO<sub>3</sub> surface modification upon low energy Ar<sup>+</sup> bombardment studied by XPS, *Vacuum* 131 (2016) 14–21, <https://doi.org/10.1016/j.vacuum.2016.05.026>.

[32] J. Zhao, Y. Li, Y. Zhu, Y. Wang, C. Wang, Enhanced CO<sub>2</sub> photoreduction activity of black TiO<sub>2</sub>-coated Cu nanoparticles under visible light irradiation: role of metallic Cu, *Appl. Catal. A Gen.* 510 (2016) 34–41, <https://doi.org/10.1016/j.apcata.2015.11.001>.

[33] W. Wang, D. Xu, B. Cheng, J. Yu, C. Jiang, Hybrid carbon@TiO<sub>2</sub> hollow spheres with enhanced photocatalytic CO<sub>2</sub> reduction activity, *J. Mater. Chem. A* 5 (2017) 5020–5029, <https://doi.org/10.1039/C6TA11121A>.

[34] T. Wang, X. Liu, C. Ma, Y. Liu, H. Dong, W. Ma, Z. Liu, M. Wei, C. Li, Y. Yan, 3D Ag/NiCo-layered double hydroxide with adsorptive and photocatalytic performance, *J. Taiwan Inst. Chem. Eng.* 93 (2018) 298–305, <https://doi.org/10.1016/j.jtice.2018.07.031>.

[35] H. Tan, Z. Zhao, W.-B. Zhu, E.N. Coker, B. Li, M. Zheng, W. Yu, H. Fan, Z. Sun, Oxygen vacancy enhanced photocatalytic activity of perovskite SrTiO<sub>3</sub>, *ACS Appl. Mater. Interfaces* 6 (2014) 19184–19190, <https://doi.org/10.1021/am5051907>.

[36] R. Singh, N. Bayal, A. Maity, D.J. Pradeep, J. Trébosc, P.K. Madhu, O. Lafon, V. Polshettiwar, Probing the interfaces in nanosilica-supported TiO<sub>2</sub> photocatalysts by solid-state NMR and *in situ* FTIR, *ChemNanoMat* 4 (2018) 1231–1239, <https://doi.org/10.1002/cnma.201800338>.

[37] F. Liu, N. Feng, Q. Wang, J. Xu, G. Qi, C. Wang, F. Deng, Transfer channel of photoinduced holes on a TiO<sub>2</sub> surface as revealed by solid-state nuclear magnetic resonance and electron spin resonance spectroscopy, *J. Am. Chem. Soc.* 139 (2017) 10020–10028, <https://doi.org/10.1021/jacs.7b04877>.

[38] H. Zhang, Y. Li, J. Wang, N. Wu, H. Sheng, C. Chen, J. Zhao, An unprecedent hydride transfer pathway for selective photocatalytic reduction of CO<sub>2</sub> to formic acid on TiO<sub>2</sub>, *Appl. Catal. B Environ.* 284 (2021), 119692, <https://doi.org/10.1016/j.apcatb.2020.119692>.

[39] H. Xu, C. Yan, R. Li, L. Song, S. Ouyang, Synergetic modulation of surface alkali and oxygen vacancy over SrTiO<sub>3</sub> for the CO<sub>2</sub> photodissociation, *Nanotechnology* 33 (2022), 085401, <https://doi.org/10.1088/1361-6528/ac38e8>.

[40] T. Takata, J. Jiang, Y. Sakata, M. Nakabayashi, N. Shibata, V. Nandal, K. Seki, T. Hisatomi, K. Domen, Photocatalytic water splitting with a quantum efficiency of almost unity, *Nature* 581 (2020) 411–414, <https://doi.org/10.1038/s41586-020-2278-9>.

[41] S.E. Boganov, R. Becerra, V.M. Promyslov, P.G. Shangin, A.V. Lalov, M.P. Egorov, R. Walsh, Photoinduced reaction of dichlorosilylene with acetylene: matrix isolation FTIR spectroscopic study, *J. Organomet. Chem.* 962 (2022), 122270, <https://doi.org/10.1016/j.jorgchem.2022.122270>.

[42] Z. Li, P. Zheng, W. Zhang, S. Gong, L. Zhu, J. Xu, F. Rao, X. Xie, G. Zhu, Constructing SrCO<sub>3</sub>/SrTiO<sub>3</sub> nanocomposites with highly selective photocatalytic CO<sub>2</sub>-to-CO reduction, *Colloid Surf. A-Physicochem. Eng. Asp.* 650 (2022), 129686, <https://doi.org/10.1016/j.colsurfa.2022.129686>.

[43] B. Yan, Q. Wu, J. Cen, J. Timoshenko, A.I. Frenkel, D. Su, X. Chen, J.B. Parise, E. Stach, A. Orlov, J.G. Chen, Highly active subnanometer Rh clusters derived from Rh-doped SrTiO<sub>3</sub> for CO<sub>2</sub> reduction, *Appl. Catal. B Environ.* 237 (2018) 1003–1011, <https://doi.org/10.1016/j.apcatb.2018.06.074>.

[44] J. Hu, L. Yu, J. Deng, Y. Wang, K. Cheng, C. Ma, Q. Zhang, W. Wen, S. Yu, Y. Pan, J. Yang, H. Ma, F. Qi, Y. Wang, Y. Zheng, M. Chen, R. Huang, S. Zhang, Z. Zhao, J. Mao, X. Meng, Q. Ji, G. Hou, X. Han, X. Bao, Y. Wang, D. Deng, Sulfur vacancy-rich MoS<sub>2</sub> as a catalyst for the hydrogenation of CO<sub>2</sub> to methanol, *Nat. Catal.* 4 (2021) 242–250, <https://doi.org/10.1038/s41929-021-00584-3>.